

Orientation Mapping of Graphene Using 4D STEM-in-SEM^{*,**}

Benjamin W. Caplins^{a,*}, Jason D. Holm^a, Ryan M. White^a, Robert R. Keller^a

^aNational Institute of Standards and Technology, Applied Chemicals and Materials Division, Boulder, CO, 80305, United States

Abstract

A scanning diffraction technique is implemented in the scanning electron microscope. The technique, referred to as 4D STEM-in-SEM (four-dimensional scanning transmission electron microscopy in the scanning electron microscope), collects a diffraction pattern from each point on a sample which is saved to disk for further analysis. The diffraction patterns are collected using an on-axis lens-coupled phosphor/CCD arrangement. Synchronization between the electron beam and the camera exposure is accomplished with off-the-shelf data acquisition hardware. Graphene is used as a model system to test the sensitivity of the instrumentation and develop some basic analysis techniques. The data show interpretable diffraction patterns from monolayer graphene with integration times as short as 0.5 ms with a beam current of 245 pA (7.65×10^5 incident electrons per pixel). Diffraction patterns are collected at a rate of *ca.* 100/s from the μm to nm length scales. Using a grain boundary as a ‘knife-edge’, the spatial resolution of the technique is demonstrated to be ≤ 5.6 nm (edge-width 25%-75%). Analysis of the orientation of the diffraction patterns yields an angular (orientation) precision of $\leq 0.19^\circ$ (full width at half maximum) for unsupported monolayer graphene. In addition, it is demonstrated that the 4D datasets have the information content necessary to analyze complex and heterogeneous multilayer graphene films.

Keywords: scanning transmission electron microscopy (STEM); scanning electron microscopy (SEM); STEM-in-SEM; 4D STEM; graphene; 2D materials

1. Introduction

Two-dimensional (2D) materials have become ubiquitous in materials science[1]. Their intrinsic mechanical, thermal, electronic, and spintronic properties are promising for the development of functional materials. Defects, however, can significantly affect these extraordinary properties[2, 3, 4, 5]. Thus, robust structural characterization methods are required for the development of 2D materials – especially in the growth/synthesis development stage. Furthermore, we argue that it is not sufficient for characterization methods to simply exist – the appropriate characterization methods must have the potential for wide accessibility such that they become routine.

The transmission electron microscope (TEM) is one of the most widely-used atomic-scale structural characterization tools used for 2D materials. In the TEM, there are three main methods used to characterize the structure of 2D materials: parallel-beam dark-field (DF) TEM,

convergent-beam four-dimensional (4D) scanning transmission electron microscopy (STEM), and high-resolution STEM. In atomic-resolution STEM, the electron probe is small relative to the interatomic distances and each atom may be resolved in real-space[6]. Atomic-resolution STEM is particularly effective at investigating point defects[7] but can be cumbersome to apply to large areas due to real-space sampling requirements. Alternatively, DF-TEM or 4D-STEM can be used to interrogate the structure using diffraction. In DF-TEM, a parallel beam is incident on the sample and an aperture is placed in the back focal plane to generate a DF image based on a particular scattering condition. A collection of these DF images corresponding to different diffraction vectors can be used to highlight defects or create grain orientation maps[8, 9]. In 4D STEM a convergent nm-sized beam is scanned across the sample and a diffraction pattern is recorded at each real-space location and saved for off-line analysis[9, 10]. A common way to analyze 4D STEM data is by creating virtual DF (vDF) images[11]. A vDF image is generated by numerically integrating the k -space coordinates over a selected region of each diffraction pattern to create (real-space) pixel intensities.

Given the ubiquity of 2D materials research and the success that TEM has had in nano-scale structural characterization, it is somewhat surprising that structural characterization of 2D materials has been almost unexplored in the scanning electron microscope (SEM). While directly re-

*Contribution of NIST, an agency of the US government; not subject to copyright in the United States.

**Commercial instruments, equipment, or materials are identified only in order to adequately specify certain procedures. In no case does such an identification imply recommendation or endorsement by NIST, nor does it imply that the products identified are the best available for the purpose.

*Corresponding Author

Email address: benjamin.caplins@nist.gov (Benjamin W. Caplins)

solving atoms in the SEM is not straightforward[12, 13, 14] there is no clear reason why nano-beam diffraction-based techniques could not be widely leveraged. After all, the nano-beam illumination conditions used in the TEM are similar to the illumination conditions in an SEM. Benefits to performing 2D material characterization in the SEM include: easier tool access – there are far more SEMs in operation than TEMs[15]; reduced knock-on damage at SEM beam energies (≤ 30 keV)[16, 17]; increased scattering – scattering cross sections increase as beam energy is reduced[18]; a larger range of length scales – the SEM can interrogate samples from nm to mm length scales; increased scattering angles – increased angular resolution.

Despite the benefits to analyzing 2D materials in the SEM, commercially available detectors are poorly suited to provide crystallographic information. Transmission imaging detectors generally integrate electrons scattered over large solid angles, making targeted diffraction-contrast imaging difficult, though not altogether impossible. For example, using commercially available diode detectors Caplins *et al.* generated orientation maps of monolayer graphene samples[19], and Schweizer *et al.* imaged dislocations in graphene bilayer samples[20]. A recently described programmable STEM detector demonstrated the ability to provide structural information on graphene samples; however, it is not yet commercially available[21, 22]. While important for demonstrating that the SEM has the capacity to characterize structure and defects in 2D materials, methods that use integrating detectors have limitations in terms of the difficulty of method implementation and the information content available.

Recently, there has been a push toward integrating on-axis diffraction cameras into the SEM which represents a leap forward in the information content available in the SEM[23, 24, 25, 26, 21, 13, 27, 28]. In theory, an SEM with an on-axis diffraction camera can be used for 4D STEM diffraction experiments. In practice, however, the commercially available detectors have not yet demonstrated that they have the necessary signal-to-noise to perform high-throughput diffraction studies on 2D materials. Generally, commercially available detectors are instead optimized/utilized for transmission Kikuchi diffraction (TKD) which is a powerful technique for characterizing thicker (3D) materials [29, 24, 30].

Herein, we describe a high-throughput scanning diffraction technique, referred to as 4D STEM-in-SEM (four-dimensional scanning transmission electron microscopy in the scanning electron microscope). In this technique, a convergent electron beam is scanned across an electron transparent sample. At each real-space position, a diffraction pattern is recorded and the resulting 4D dataset, $I(x_r, y_r, x_k, y_k)$, is saved to disk for off-line analysis. Note that the r and k subscripts denote the real and reciprocal-space coordinates respectively. Using polycrystalline and heterogeneous graphene films as representative 2D material test samples, we demonstrate and discuss a few of the many ways to utilize the 4D dataset. During the

preparation of this manuscript a similar 4D STEM-in-SEM method applicable to 2D materials was described by Schweizer

et al.[28]. A discussion of the differences between the approaches is included at the end of the manuscript.

2. Methods

A schematic of the 4D STEM-in-SEM setup is shown in Figure 1. An SEM (Zeiss Gemini 300) scans a 30 keV convergent electron probe across an electron transparent graphene sample mounted on a custom sample holder. The electrons transmitted through the sample propagate in a field-free region and strike a phosphor screen (nominally P43, 1 μm - 2 μm grain size, 10 μm - 15 μm thickness, 25 nm - 50 nm Al top coat) which emits photons. The resulting optical diffraction pattern is imaged out of the vacuum chamber onto a CCD camera (Thorlabs 1500M-GE). The optical assembly is described in detail elsewhere (the changes from the previous description[22] are that the digital micromirror device was replaced with a CCD and the YAG:Ce screen was replaced by a P43 phosphor).

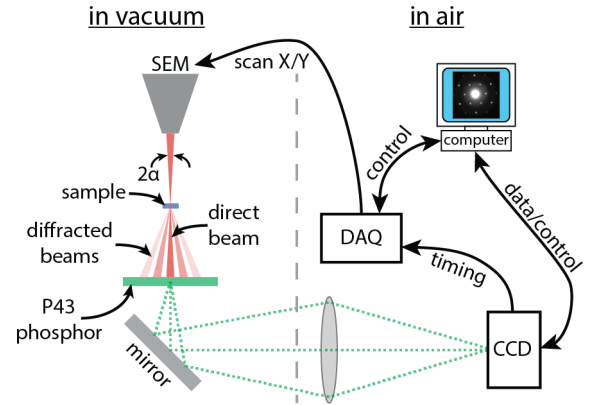


Figure 1: A schematic of the 4D STEM-in-SEM experimental setup. The electron beam with convergence semiangle α is focused on a graphene sample. A phosphor screen is positioned beneath the sample. The electrons that transmit the sample strike the phosphor and generate photons forming an optical diffraction pattern. The diffraction pattern is then imaged onto a CCD camera located outside the vacuum chamber. To collect a 4D dataset, a computer controlled data acquisition device scans the electron beam synchronously with the collection of frames from the CCD. The data is saved to disk for off-line analysis.

The electron beam was scanned across the sample by driving an external scan generator input with a multifunction data acquisition device (National Instruments, LabVIEW, USB-6351)[31]. The CCD has a global shutter and frame buffer and was operated in ‘overlapped exposure’ mode using the falling edge of the ‘strobe’ camera output as the trigger for stepping the electron beam position. For simplicity, a standard raster pattern with no flyback time was used for scanning; for the dwell times used here (ms

time scale), significant scan artifacts were not observed[31]. Using this timing protocol, diffraction patterns from consecutive pixels were not mixed beyond that which occurs due to the P43 phosphor decay time[32].

Camera data were streamed to the control computer and saved to disk in real-time. For most data presented here, a $4 \text{ px} \times 4 \text{ px}$ binning (hardware vertical binning), 40 MHz pixel clock, and a $400 \text{ px} \times 400 \text{ px}$ region of interest (ROI) was used on the CCD camera (resulting in $100 \text{ px} \times 100 \text{ px}$ diffraction patterns). For large real-space fields-of-view (FOVs) such as Figure 4a a larger ROI was selected to accommodate the movement of the diffraction pattern on the detector that occurs due to the scanning of the electron beam. For higher quality/resolution diffraction patterns (such as Figure 8c-d), no binning was used. The image collection rate was generally limited by the camera readout electronics (not the exposure time) and depending on the ROI, binning, and pixel clock it ranged from 30 patterns/s (data in Figure 8) to 108 patterns/s (data in Figure 3). To collect as much signal as possible while ensuring minimal mixing of the diffraction patterns at different beam positions (due to the P43 phosphor decay time) the exposure time was set to be *ca.* 1 ms less than the inverse of the readout-limited rate; this allows 1 ms between the movement of the beam and the start of the next exposure. With the exception of the data in Figure 8, all data was collected using the following beam parameters:¹ 245 pA beam current, $\alpha = 9.7 \times 10^{-4}$ rad, *ca.* 9 ms exposure time. Camera gain and dark level were adjusted as needed.

Most datasets presented here were collected with a real-space scan size of $512 \text{ px} \times 512 \text{ px}$, resulting in a 4D dataset acquisition time of *ca.* 40 minutes. No drift corrections were applied. The uncompressed 4D datasets ranged from 32 GB to 10 GB in size. Data analysis was performed using custom scripts (Mathworks, Matlab). Data and analysis methods are available upon reasonable request. The total processing time to go from the raw 4D datasets to the data presented in this manuscript was <60 minutes on a desktop computer (6 cores @ 3.5 GHz, 128 GB RAM) and no run-time optimization was pursued.

3. Results

Figure 2 shows example diffraction patterns collected from a monolayer graphene film supported on a Quantifoil TEM grid (Graphenea). Using a relatively long (250 ms) exposure time without any pixel binning, several orders of diffraction spots are visible as well as diffuse rings from amorphous contaminants. Diffraction patterns collected

with significantly shorter exposure times require pixel binning to maintain adequate signal-to-noise. Using 0.5 ms exposure times, the first two orders of diffraction spots are visible from monolayer graphene using $4 \text{ px} \times 4 \text{ px}$ binning. From a practical perspective, the data-transfer rate is limited to *ca.* 108 patterns/s by the camera electronics and so exposure times less than 8 ms were not used to collect 4D datasets.

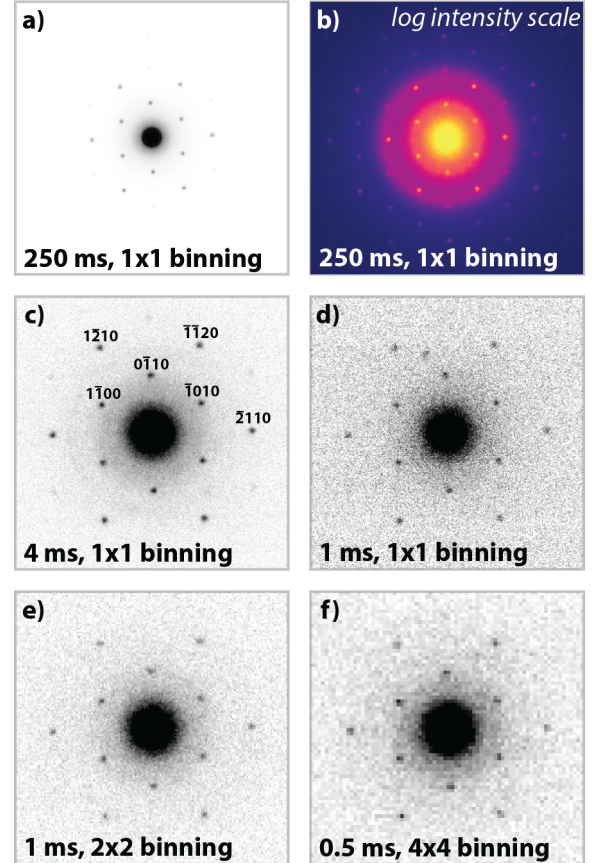


Figure 2: Diffraction patterns collected from monolayer graphene with different exposure times and binning conditions. In (c) the diffraction spots are indexed. The beam current was 245 pA with $\alpha = 9.7 \times 10^{-4}$ rad. Diffraction spots from graphene are still visible using an exposure time of 0.5 ms. Note that the achievable frame rate with the CCD is slower than the inverse of the exposure time for (c-f) due to pixel read/transfer limitations – i.e. the data in (f) was not collected at 2 kHz.

¹In this work we used the ‘high-current’ mode on our SEM, which serves to increase the beam current while decreasing the electron beam convergence angle. In general, electron beam parameters that yield high depth-of-field will correspond to smaller convergence angles and will give ‘spot’ diffraction.

ing) with a Gaussian mask where the width of the Gaussian is chosen to correspond to the width of the saturated area of the detector. Once the centers of all the diffraction patterns are located, the pixel coordinates of the direct beam are fit to a plane using a trimmed least-squares method and used to locate the center of each diffraction pattern with high precision.

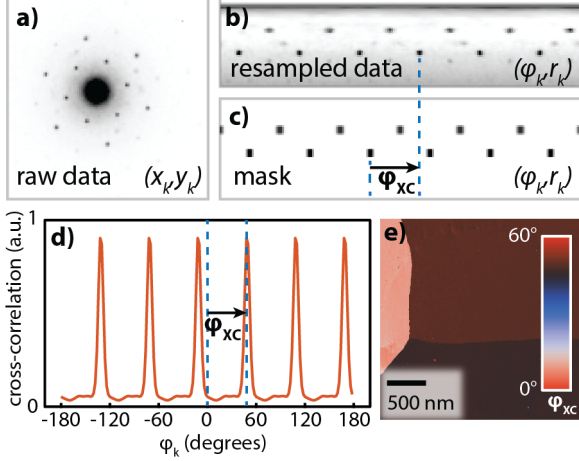


Figure 3: The work-flow used for creating an orientation map from a 4D STEM-in-SEM dataset. (a) An example diffraction pattern collected in a 4D STEM-in-SEM dataset. Note that the direct beam is not centered in the FOV. (b) The diffraction pattern is resampled from Cartesian (x_k, y_k) to polar (ϕ_k, r_k) coordinates. (c) A mask with the same symmetry as the graphene diffraction pattern is used in a cross-correlation (i.e. template matching) analysis. (d) The value of the cross-correlation between the diffraction data and the mask is plotted. By construction, the mask is six-fold symmetric and consequently so is the cross-correlation. The maximum value of the cross-correlation on the interval $\phi_k \in [0^\circ, 60^\circ)$, denoted ϕ_{XC} , is taken as a measure of the graphene lattice orientation (relative to the mask). (e) The orientation of the full example 4D dataset is plotted using a circular colormap. Here, the graphene film consists of three grains that meet at a triple point.

Given the six-fold rotational symmetry of a graphene diffraction pattern[36] (assuming the beam is at normal incidence to the graphene), it is useful to resample the diffraction patterns from Cartesian coordinates to polar coordinates for orientation analysis[37]. Using the position of the direct beam, each diffraction pattern is numerically resampled from Cartesian (x_k, y_k) to polar (ϕ_k, r_k) coordinates (Figure 3b); the appropriate Jacobian factor is applied such that the total intensity is conserved between the two representations of the dataset.

There are numerous ways to calculate the orientation of graphene given the diffraction pattern. In the interest of simplicity and while also making full use of the symmetry of the diffraction pattern, we use a mask-based cross-correlation (i.e. template matching) approach (Figure 3c). Here, a mask is generated by using flat-top super-Gaussian diffraction spot profiles. The center of each spot profile in the mask was determined by the calculated diffraction pattern of graphene, and the widths were estimated by visual inspection. No effort was made to optimize the mask. The

primary goal when creating the mask was to ensure that it had the appropriate structure/symmetry and was smooth.

To determine the lattice orientation, the resampled diffraction data for each pixel was cross-correlated along the ϕ_k -dimension with the generated mask. A sub-pixel cross-correlation algorithm[35] was used to find the maximum of the cross-correlation coefficient on the interval $\phi_k \in [0^\circ, 60^\circ)$; the location of the maximum was taken as a measurement of the graphene lattice orientation relative to the mask, ϕ_{XC} (Figure 3d). Finally, an orientation map is constructed by associating the ϕ_{XC} determined at each pixel with a circular colormap[38]. Figure 3e shows an examined region with three distinct grains meeting at a triple point.

A significant benefit in using 4D STEM-in-SEM for grain orientation analysis is that it can interrogate a wide range of length scales. Figure 4 and 5 show conventional secondary electron (SE) images and 4D STEM-in-SEM derived orientation maps for six nested FOVs spanning millimeters to nanometers. Each dataset was collected at $512 \text{ px} \times 512 \text{ px}$ resolution with FOVs of $2250 \mu\text{m}$, $546 \mu\text{m}$, $159 \mu\text{m}$, $38 \mu\text{m}$, $9.50 \mu\text{m}$, and $2.37 \mu\text{m}$. Thus, the data give information on length scales from *ca.* 2 mm to 4 nm. This range of length scales is something that, to our knowledge, is not readily accessible using other techniques.

At the largest FOV (Figures 4a, 5a) the full TEM grid can be identified in both the SE image and orientation maps. For the regions of the TEM grid that are not electron transparent (i.e. the grid bars), the orientation map is colored beige. At the largest FOV, the orientation data appears as random noise because the step size is on the same order of magnitude as the grain size. However, as the FOV is decreased, the individual grains become observable. At smaller FOVs (Figures 4c-f, 5c-f) the SE images show strong contrast between the unsupported graphene and the Quantifoil (carbon) support film, however, there is no clear contrast in the orientation maps. This demonstrates the graphene orientation can still be quantified even though the scattering of interest arises from monolayer graphene on top of a much thicker amorphous carbon substrate. For reference, the atomic area density of graphene is 38 atoms/nm^2 while 12 nm of amorphous carbon (nominal thickness of a Quantifoil support) has a projected area density of 1325 atoms/nm^2 (assuming $\rho = 2.2 \text{ g/cm}^3$). For the smallest FOV, the SE images show contrast on the 50 nm length scale which we attribute to contaminants[39]. Note that the contrast in the SE image is not apparent in the orientation map because the orientation analysis is designed to be sensitive to the graphene spot diffraction signal rather than the diffuse signal from the substrate and contaminants.

For demonstration purposes the inset of 5c shows a grain size distribution for the data in 5c. Here ‘grain size’ is defined as the equivalent circular diameter. Notably, in only a single automated scan, 917 individual grains were identified and quantified leading to relatively robust statistics ($2.6 \mu\text{m} \pm 0.2 \mu\text{m}$). The segmentation algorithm used

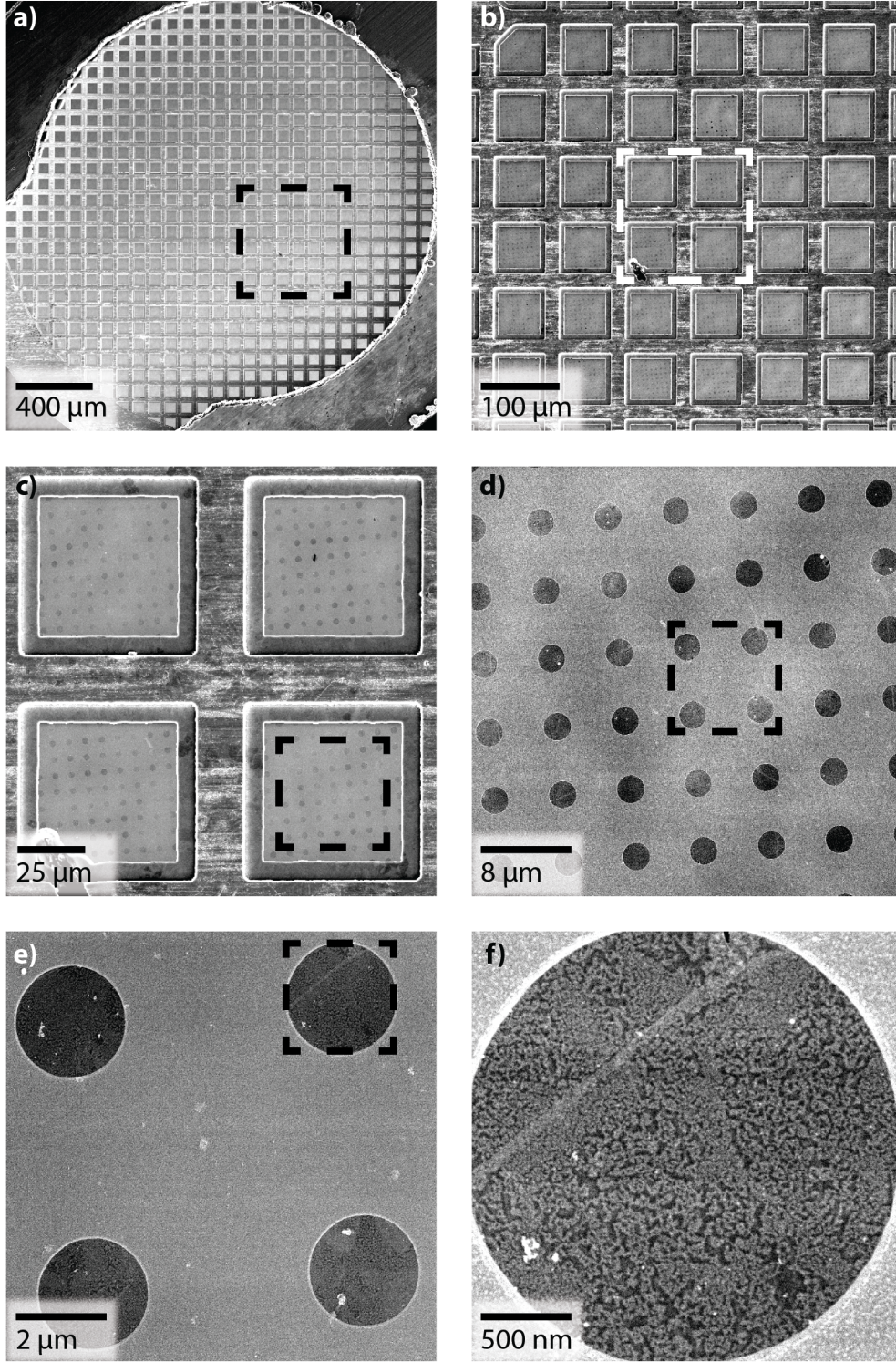


Figure 4: Conventional secondary electron (SE) images of nominally monolayer graphene on a Quantifoil TEM grid. The SE images are all of the same sample and were collected in the order presented. Each subsequent FOV is marked with a dashed box and is approximately 4X smaller. The FOVs are 2250 μm , 546 μm , 159 μm , 38 μm , 9.50 μm , and 2.37 μm . In (a) the majority of the TEM grid is visible. In (c) both the grid bars and support film are visible. In (f) the support film is visible at the corners of the FOV and the unsupported graphene can be inferred in large part because of the debris that is scattered across the surface.

to generate this grain size distribution was not rigorously tested for accuracy and so the data is for demonstration

purposes only.

One problem with the analysis method outlined above

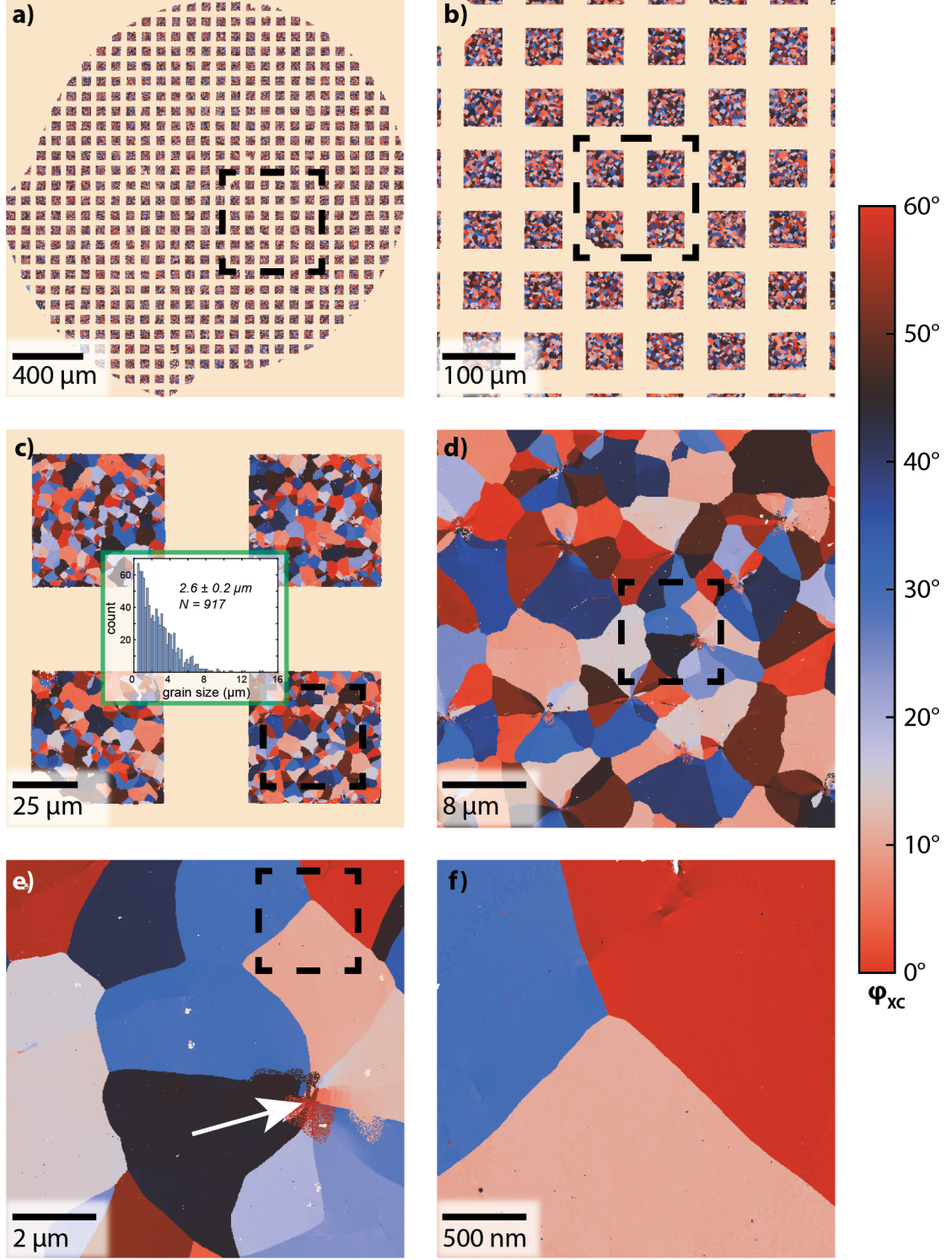


Figure 5: Orientation maps of graphene corresponding to the same FOVs shown in Figure 4. Here the regions of the TEM grid that are opaque to electrons are colored beige. In (a) the orientation data looks like noise because the step size is larger than the grain size. In (c) the grains become well defined. In (f) the grain size is similar to the FOV and a triple point is visible. The arrow in (e) highlights a speckled region that is an artifact in the orientation map due to the presence of multilayer graphene which is discussed in Figure 7. A careful inspection of (d) reveals more artifacts like that indicated in (e). For demonstration purposes, the inset in (c) shows the grain size distribution for that data where ‘grain size’ is defined as the equivalent circular diameter.

is that it uses a mask that assumes the diffraction arises from monolayer graphene. Thus, for multilayer regions

which are routinely observed in CVD grown graphene samples[40], the orientation map is ill defined – i.e. the

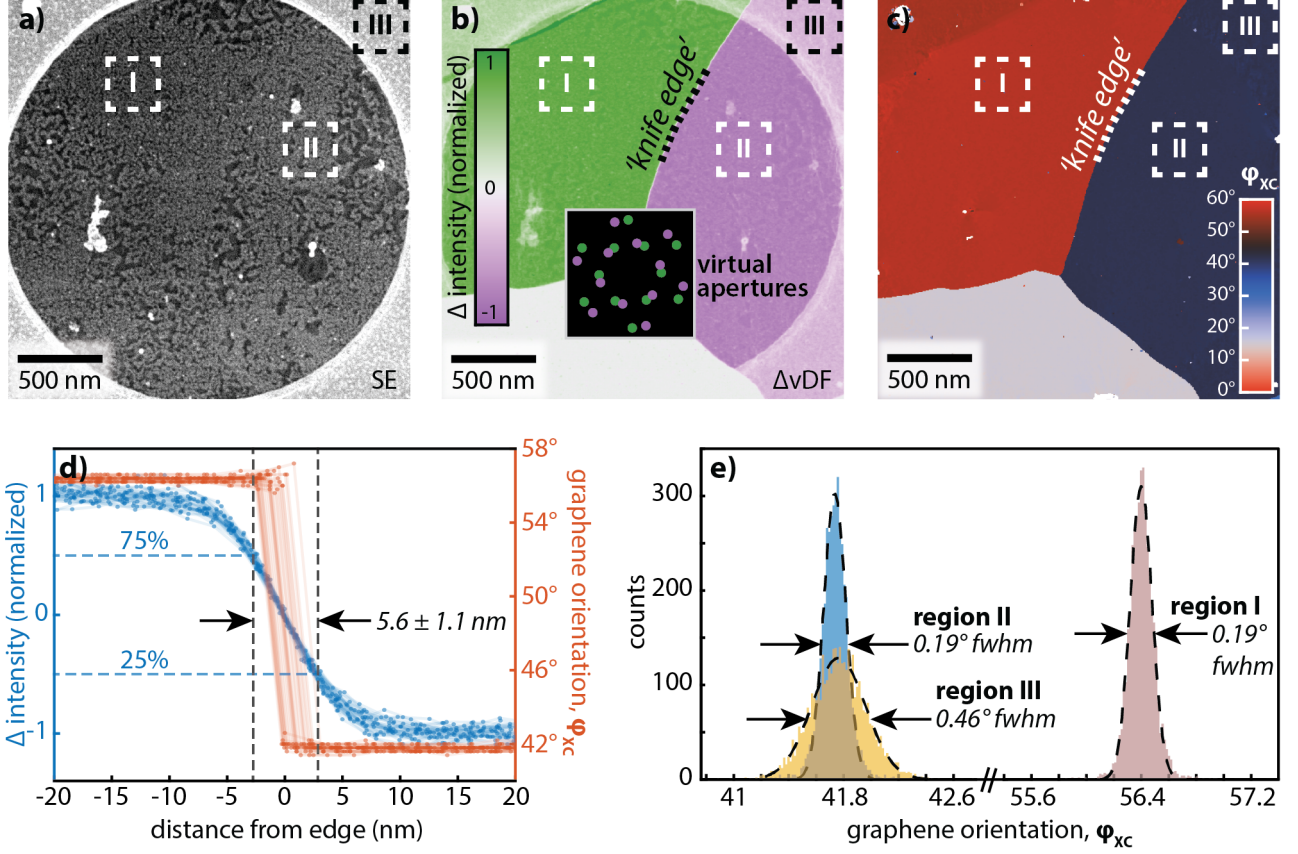


Figure 6: (a) An SE image of monolayer graphene. The amorphous carbon support film is visible at the corners of the FOV. (b) A ΔvDF image of the same FOV corresponding to the difference between two vDF images. The virtual apertures associated with the two DF images are color-coded and shown in the inset. The ΔvDF image minimizes the contribution of amorphous debris to the diffraction patterns and enhances the grain boundary used as a ‘knife edge’. (c) The corresponding orientation map. (d) Horizontal line scans across the knife edge. The intensity-based ΔvDF line scans are shown in blue and have a smooth shape with a measured edge resolution of 5.6 nm (25% to 75%). The orientation-based line scans are shown in orange and show step-like behavior because they are primarily limited by the step size used (2.3 nm). (e) Histograms of the orientation measurements made for each pixel in regions I, II, and III which are indicated in (a-c). The FWHM of the histograms from the unsupported graphene in regions I and II is 0.19° and may be taken as an upper bound on the angular precision of a single measurement. The precision is slightly degraded to 0.46° in region III by the presence of the amorphous support film.

algorithm will return a value for the orientation, but for misaligned bilayers, the orientation that the algorithm selects tends to jump between the two graphene lattice orientations depending on the exact diffraction efficiency of the probed region and the noise. An example is indicated in Figure 5e with an arrow; more examples can be seen in Figure 5d. Neither the SE images nor the orientation maps shown in Figure 5 clearly identify these multilayer regions leading to ambiguity of interpretation. Later, we will discuss a method to identify and classify these regions using a diffraction-amplitude based analysis (*vide infra*).

A natural question that arises in orientation analysis is: What is the spatial resolution and angular precision of the technique? To answer the spatial resolution question, a grain boundary was used as a ‘knife-edge’ – i.e. we assume that a grain boundary is an atomically ‘sharp’ step in orientation.² First, a well-defined grain boundary in monolayer graphene was located in the sample. The SE

image (Figure 6a) only shows contaminants and the support film[39]. No significant thickness or topographic features were evident. Next, two vDF images were created[11] corresponding to the diffraction intensity of the two adjacent graphene grains; these vDF images were then subtracted to create a difference image (ΔvDF) that removes much of the amorphous contribution (Figure 6b). The orientation map for the same FOV (Figure 6c) was generated using the mask-based method. Then, 32 horizontal scans across the grain boundary were collected using a 2.3 nm step size. Each horizontal scan across the grain boundary was fit to an error function and aligned to have the same inflection point (Figure 6d). The distance required to go from 25% to 75% of the step intensity is measured to be 5.6 nm \pm 1.1 nm and is assumed to be due to a combination the electron beam spot size and environmental noise. In

that for thicker samples it is necessary to pick a grain boundary that is parallel to electron beam to ensure the knife-edge is ‘sharp’.

²Although for monolayer graphene this is not an issue, we note

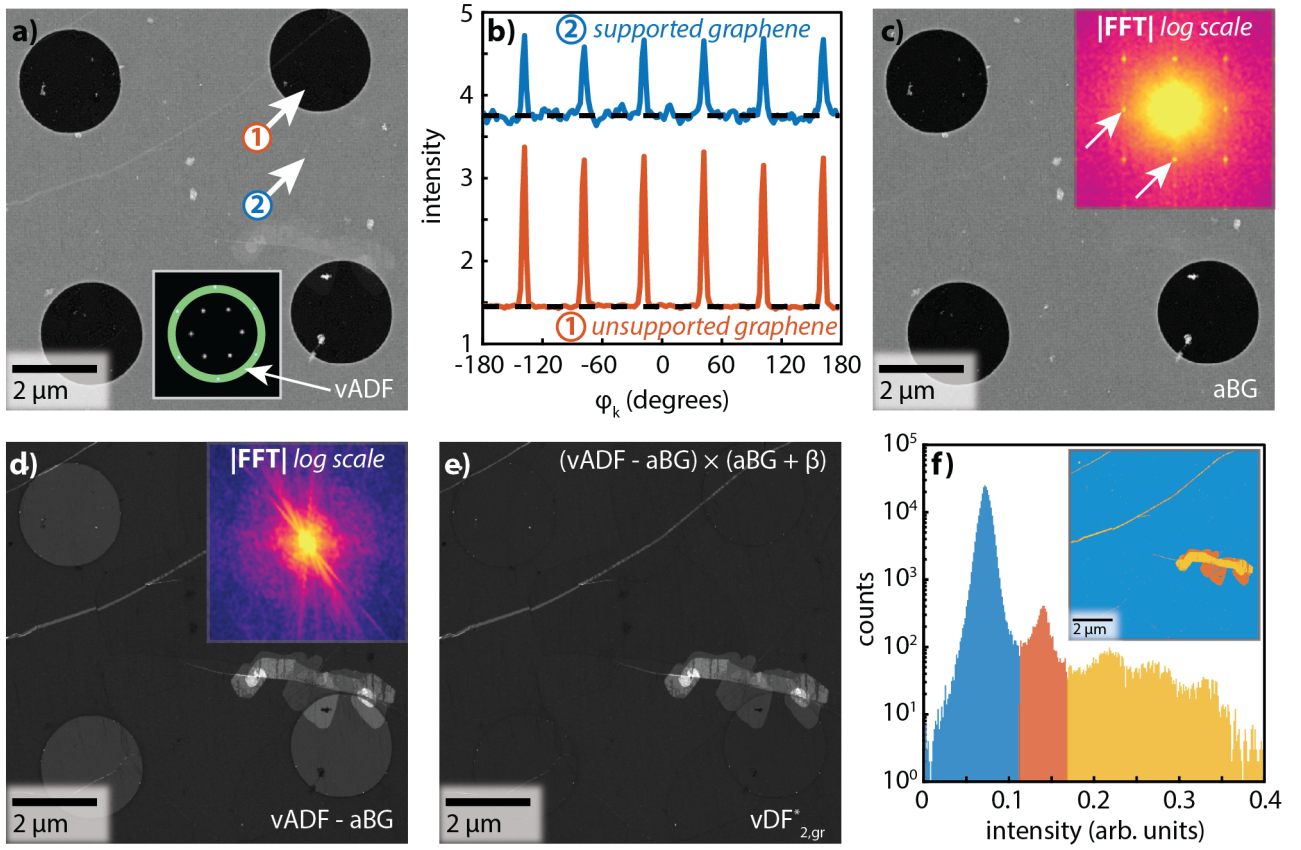


Figure 7: (a) A vADF image; the annular virtual aperture used is shown in the inset overlaid on the diffraction expected for graphene. The contrast is dominated by the support film. (b) The diffraction intensity along the annular slice through the diffraction pattern collected at the two locations indicated in (a). The diffraction from the unsupported graphene has a low baseline (amorphous contribution) and tall peaks (graphene contribution). The diffraction from the supported graphene has a higher baseline and shorter peaks due to the support film and multiple scattering. (c) The contribution to the vADF image from the baseline scattering (amorphous background). The inset 2D power spectrum shows clear peaks caused by electron beam contamination from a previous (*ca.* 4X lower magnification) scan. (d) The image that results from subtracting (c) from (a); here the background scattering is removed and the contrast predominately comes from graphene diffraction. The inset 2D power spectrum shows that the contribution from the electron beam contamination has been removed. (e) The image that results from performing a first-order multiple-scattering correction on (d). Here the image is interpretable as diffraction contrast from graphene without being significantly affected by the support material. (f) The intensity histogram of (e) that shows discrete peaks corresponding to different thicknesses of graphene which can be thresholded. The inset shows the thresholded image.

this case, the horizontal scan direction is not exactly perpendicular to the grain boundary leading to a geometrical increase of the measured edge width. This geometrical effect can be corrected by multiplying by the cosine of the angle [$\cos(26^\circ) = 0.90$] to get an effective edge width (25% - 75%) of $5.0 \text{ nm} \pm 1.0 \text{ nm}$. The diffraction-limited resolution ($0.61 \cdot \lambda/\alpha$) for the electron beam used here is 4.4 nm [41]. The 2.3 nm step size yields a 4.6 nm Nyquist resolution limit. It is not meaningful to directly compare the edge width, the Airy disk, and the Nyquist resolution limit, so we translate the former two measurements into their equivalent Gaussian width (2σ). The edge measurement yields a 2σ resolution of $7.4 \text{ nm} \pm 1.5 \text{ nm}$, and the diffraction limit yields a 2σ resolution of 3.1 nm [42]. Thus, the observed resolution is 1.6X the Nyquist limit for this measurement and 2.4X the diffraction limit. Chromatic aberration, spherical aberration, and ambient noise sources contribute to this discrepancy.

The previous resolution discussion was based on the

shape of the *intensity* line scans. In contrast, for large changes in the graphene orientation as shown in Figure 6d, the precision in the graphene *orientation* measurement (i.e. an angular measurement, not an intensity measurement) is effectively limited only by the electron beam step size (2.3 nm). In summary, the resolution of grain boundaries is measured to be roughly 2X poorer than the fundamental limits (diffraction and discretization), but an isolated grain boundary can be located to within the step size used (2.3 nm).

The angular precision is quantified in Figure 6e. Here, the histogram of orientation angles is plotted for the three regions indicated in Figure 6c. For regions I and II the distribution has a full width at half maximum (FWHM) of 0.19° . Region III has a notably wider orientation distribution with a FWHM of 0.46° . Assuming that the regions are orientationally homogenous, then these FWHMs represent the angular precision of the technique as limited by the CCD pixel size, the signal-to-noise in the diffraction

pattern, and the analysis algorithm used. Residual strain or defects in the graphene will serve to broaden these measurements and so these angular precision measurements may be taken as an upper bound on the true measurement precision. The effect of having a significant background in the diffraction pattern due to the amorphous carbon support material can be seen in the modestly increased FWHM of the region III histogram.

While the diffuse scattering from the amorphous carbon and polymer debris/residue has only a modest deleterious effect on the orientation measurement, it can significantly degrade the ability to interpret virtual annular dark field (vADF) images. Figure 7a shows a vADF image formed by using an annular mask centered on the 2nd order diffraction spots of graphene. Ideally, this image would selectively highlight the thickness of the graphene sheets, however, the diffuse scattering from the support material overwhelms the graphene diffraction signal. Because the full 4D dataset is available, this amorphous contribution can be removed. Figure 7b shows the annular diffraction data plotted as a function of angle, ϕ_k , from the diffraction patterns collected at the two locations indicated in Figure 7a. The graphene on top of the amorphous support film has a significantly higher background and less intense graphene diffraction peaks than the unsupported graphene. The vADF image (Figure 7a) was formed by integrating the area under these curves, thus it is readily seen that the integrated diffraction signal from graphene is small compared to the integrated scattering signal from the support film. Thus, the amorphous contribution dominates the vADF images. To isolate the contrast due to diffraction from the graphene lattice, the amorphous background (aBG) contribution (i.e. the baseline) to the signal (Figure 7c) is subtracted from the original vADF image (Figure 7a). The resulting image (Figure 7d) has significantly enhanced contrast from graphene related diffraction and the folds/wrinkles and multilayers become apparent. Residual contrast is still visible due to the support material, however. To first order, this residual contrast can be attributed to multiple scattering effects – i.e. as the amorphous scattering removes intensity from the direct beam, the diffracted spots become proportionally less intense. If we ignore an arbitrary overall scale factor then we can correct (to first order) the image by multiplying the background-corrected image by a linear function of the amorphous background:

$$vDF_{2,gr}^* = (vADF - aBG) \times (aBG + \beta)$$

Here we refer to the amorphous-background and multiple-scattering corrected DF image as $vDF_{2,gr}^*$; the subscripts emphasize that we are isolating the signal from the second order diffraction spots of the graphene lattice and the asterisk denotes that the data has been corrected – i.e. it is no longer the simple projection of the 4D dataset typically referred to as a vDF image[11]. The parameter, β , is determined by minimizing the residual contrast

between the supported and unsupported portion of monolayer graphene. The $vDF_{2,gr}^*$ image is shown in Figure 7e and shows thickness contrast with almost no remaining contrast from the support film. The histogram generated from this image (Figure 7f) shows peaks corresponding to different graphene thicknesses and the image can be thresholded if desired; this is useful for masking the orientation maps which assume monolayer graphene. Note that Figure 7 shows the same FOV as Figure 4e and 5e. Thus, the previously noted ambiguity in the orientation maps due to multilayer graphene can be identified and removed if necessary. The efficacy of the amorphous background signal removal procedure can be seen indirectly in the 2D power spectrum of the aBG image and the background corrected vADF image (Figure 7c-d). The power spectrum of the aBG image shows peaks that correspond exactly to the raster pattern from a previously recorded image; these arise from electron beam contamination accumulated during the previous scan’s pixel dwell time. After subtraction of the amorphous background contribution, the 2D power spectrum no longer shows these peaks.

It is important to note that while the intensity histogram of the amorphous background corrected image shows distinct maxima, care must still be used interpreting these images – i.e. the maxima cannot be blindly interpreted as monolayer/bilayer/trilayer/etc. Tilts/roughness of the graphene film affects the diffraction intensity[36, 10] in addition to the layer stacking/twist angle[43, 44]. These effects will manifest in the 4D dataset however and can be disentangled with appropriate analysis.

Finally, we demonstrate the information content accessible in 4D STEM-in-SEM for a more complex graphene sample. The sample used in Figure 8 is nominally bilayer graphene, but the FOV exhibits folds/wrinkles and multilayers. The $vDF_{2,gr}^*$ image is shown in Figure 8a. Analyzing such a heterogeneous dataset is beyond the scope of this manuscript, however, we emphasize that the 4D dataset contains the information necessary to analyze this FOV in detail. For example, two diffraction patterns are shown in Figure 8c-d. The diffraction pattern collected at the first location is from a monolayer region of graphene, while the diffraction pattern collected at the second location shows seven different graphene orientations are present. For a rapid model-free visualization of the data we use a method developed in a previous work that creates a colorized map of the amplitude of the first three circular moments of the data (Figure 8b) which is useful for generating qualitative contrast based on the structure of the diffraction pattern (see Ref [19] for details). Here the structural heterogeneity is quite apparent. A more detailed analysis yielding layer number and orientation angles of each diffraction pattern in the 4D dataset should, in principle, be possible using this data.

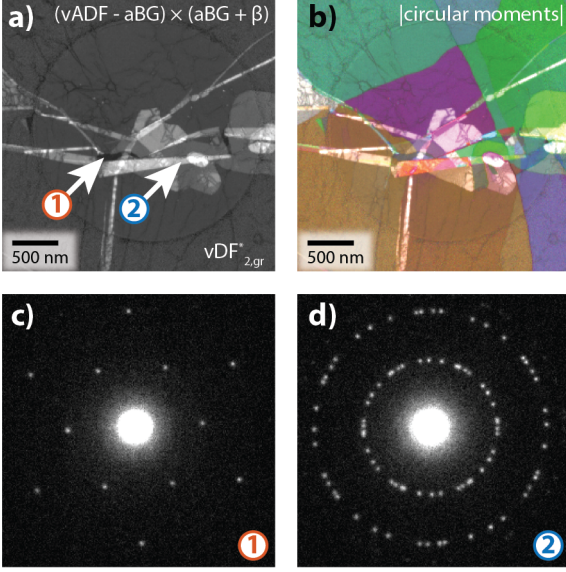


Figure 8: (a) An amorphous-background and multiple-scattering corrected vADF image ($vDF_{2,gr}^*$) of a nominally bilayer graphene film. Despite being nominally bilayer, this FOV shows a significant amount of heterogeneity. (b) A colorized image designed to emphasize thickness and orientational heterogeneity. See Ref [19] for details on the colorization algorithm. (c) The diffraction pattern collected at location 1 indicated in (a); this diffraction pattern is assigned to monolayer graphene. (d) The diffraction pattern collected at location 2 indicated in (a); this diffraction pattern shows seven unique graphene orientations. The 4D dataset used in this Figure was collected with a 30 ms exposure time, without pixel binning, and with a small beam-limiting aperture ($\alpha \approx 3 \times 10^{-4}$ rad, $I_{beam} = 14$ pA).

4. Discussion

The 4D STEM-in-SEM technique we described is capable of performing characterization of graphene from the nm to mm length scale. We demonstrated a fully automated measurement that generates high-precision orientation maps in monolayer graphene, and, has the information content necessary to analyze multilayer samples. Additionally we described one example of how the 4D dataset can be used to correct diffraction contrast images for amorphous-background and multiple-scattering, increasing the interpretability of DF images beyond what is possible with a traditional DF image (virtual or not).

In this work we have chosen a single set of experimental conditions in order to demonstrate the technique, however, it is worth commenting on how these choices affected the data. First and foremost, the beam energy determines the scattering cross section, scattering angles, and detective quantum efficiency (DQE). Using a lower beam energy will increase the scattering cross sections and scattering angles at the expense of lowering the DQE (because of the energy dependent photon yield of the phosphor). For the data collected in this manuscript on graphene, we prioritized DQE which led us to use a 30 keV beam. Next, as mentioned, we used the ‘high current’ mode on the microscope which (for a given beam limiting aperture) re-

duces the convergence semi-angle significantly (improving the angular resolution), while causing the achievable spatial resolution to deteriorate. The tradeoff between spatial resolution and diffraction spot width is the same as experienced in nano-beam diffraction in the TEM. Additionally, for extremely thin samples such as graphene, the total electron dose must be considered because of the contamination associated with it – higher currents may not necessarily be advantageous. Finally, the choice of phosphor, image relay optics, and camera will affect the k-space resolution, DQE, and achievable frame rate. For strongly scattering samples we prefer Ce:YAG scintillators for higher clarity of the diffraction pattern and faster decay time, however, for weakly scattering samples such as graphene the P43 phosphor has a higher photon yield. In general, for weakly scattering samples (like graphene) the experimental conditions should be optimized with the sample in mind.

To our knowledge, there is only one other effort in the literature to bring 4D STEM to the SEM with application to 2D materials. Schweizer *et al.* developed a technique termed low energy nano diffraction (LEND)[28]. In LEND, a phosphor screen is placed below a sample and an off-axis camera placed in the vacuum chamber is used to view the diffraction pattern on the screen from above the sample plane. The strong benefit of this setup is that it is simple to implement and only uses low-cost commercially available components that should be compatible with many different manufacturer’s SEMs. Additionally, it seems to work at low beam energies (500 eV). For many users, having direct access to the diffraction pattern from a sample would be well worth the investment.

However, a low-cost camera placed off-axis and in-vacuum is not without disadvantages. First, placing the camera in vacuum places severe limitation on the size of the camera that can be used; scientific-CMOS (or CCD) cameras are significantly larger than board-level industrial-quality machine vision cameras. The small form-factor camera used in the LEND setup has a rolling shutter, small pixel size (which typically result in higher noise levels due to pixel read noise), and a low overall quantum efficiency (in large part due to the Bayer color filter). Additionally, although noise specifications are not provided by the manufacturer for the camera used in the LEND setup, it is reasonable to assert that the read-noise is significantly higher than that of a scientific-grade CMOS/CCD camera; read-noise is particularly important in low signal applications such as high-speed diffraction measurements.

An additional feature to be considered with the LEND setup is that the off-axis geometry imparts a significant non-rotationally-symmetric geometric distortion to the collected diffraction pattern which must be taken into account during analysis. Due to the significantly tilted object plane, a small aperture lens must be used to keep the object plane in adequate focus (which gives a large depth of field and reduces the collection efficiency) or a more complex lens assembly must be used that compensates

for the tilted object plane by adhering to the Scheimpflug principle[45]. This distortion could be problematic if strain and tilt mapping is to be performed[10]. Thus, while the LEND setup has significant promise to bring diffraction methods to more SEM users, it is (at least in its current manifestation) not particularly well-suited to high-speed orientation mapping of weakly scattering samples.

In contrast to LEND, the experimental setup used in this work employs a rotationally-symmetric on-axis lens assembly with relatively high numerical aperture[22]. Furthermore, since the camera is placed outside the vacuum chamber, the size and quality of the camera can be selected to fit the experimental needs, as opposed to the space constraints of the SEM vacuum chamber. Here, we used a scientific-grade monochrome CCD camera removed from a decommissioned electron backscatter diffraction (EBSD) detector that is only of moderate quality in terms of its low-signal high-speed imaging performance in comparison to modern scientific CMOS cameras. Modern high-performing scientific CMOS cameras would enable this method to achieve a frame rate of 10^3 frames/s, similar to current EBSD detectors[46]. With regard to LEND, we also anticipate that advances in sensor/camera technology will bring higher quality cameras to the small form factor needed for that technique. Finally we note that the LEND setup uses a P22G phosphor while the 4D STEM-in-SEM setup uses a P43 phosphor. P22G may be a better phosphor choice in terms of photon yield and decay time[47]. However, side-by-side testing would need to be performed to clearly identify the benefits and drawbacks to these different phosphors.

We know of only two other detectors that have collected (on-axis) 4D STEM-in-SEM datasets, albeit not on 2D materials. One is the Optimus detector that is designed for TKD and is optically similar to the 4D STEM-in-SEM detector we describe here[24]. The other is an on-axis Timepix-based direct electron detector that was used to create vDF images of some nanomaterials[25].

At this point it is worth considering the question:

Why are we developing 4D STEM-in-SEM?

After all, some would say that nano-beam 4D STEM(-in-TEM) already exists[48] and the hardware in a TEM is generally of higher quality than in an SEM (i.e. more & better electron lenses, improved stability, more mature detector technology, etc). We argue that there are many compelling reasons to develop 4D STEM-in-SEM. First and foremost, the low beam energies found in an SEM *improve diffraction contrast* (higher scattering cross sections) while eliminating knock-on damage in all but the most beam sensitive samples (i.e. low atomic number atoms – such as Li – in weak bonding environments).

Another answer is that the range of length scales that can be interrogated in an SEM is *significantly* larger than in a TEM and should lead to more representative sampling statistics. One more answer is that the SEM vacuum chamber is *spacious* and allows for easier integration of

accessories enabling *in-situ* and multimodal experiments with relative ease. For instance, tensile stages, nanomanipulators, heating stages, optical assemblies, etc are all easily accommodated in an SEM. Yet another answer is related to the *accessibility* of the technique. For example, at present, although the TEM can generate orientation maps of 2D materials, orientation maps are simply not standard in 2D material growth manuscripts. In our view, this represents a deficiency that, if corrected, could accelerate advancements in 2D materials synthesis techniques and applications. We hope that 4D STEM-in-SEM will improve the accessibility of orientation/texture measurements of 2D materials much in the same way that EBSD/TKD improved the accessibility of orientation/texture measurements of 3D materials.

Finally, we consider ways to improve the experimental approach used here. Small changes such as using a better (i.e. faster, lower noise, higher dynamic range) camera, increasing the numerical aperture of the lens system, and using a faster and/or brighter phosphor will certainly improve the method in the short term. Collecting 4D STEM-in-SEM datasets at a > 1 kHz framerate is not unreasonable given current camera technology[46]. However, in the long term, the sensitivity, readout speed, and dynamic range possible with a direct electron detectors[49] will be highly desirable, provided that the cost associated with these detectors can be reduced. It is promising that direct electron detectors are now starting to be incorporated into EBSD detectors[50, 51, 52, 53, 54]. With a direct electron detector many of the measurements performed on state-of-the-art (nano-beam) STEM-in-TEM instruments should be viable on many field emission SEMs[10].

5. Conclusions

A 4D STEM-in-SEM experiment has been described and used to analyze graphene samples. The detector uses free-space optics to couple a phosphor to a CCD camera that is used to collect a diffraction pattern at each point on the sample. The resulting dataset is 4 dimensional, $I(x_r, y_r, x_k, y_k)$, and supports off-line analysis methods not possible with conventional SEM detectors. Using moderate beam currents it was shown that < 1 ms integration time is sufficient to collect graphene diffraction patterns with meaningful orientation information; therefore, orientation mapping of graphene in excess of 1000 points/s is possible in the SEM. Four-dimensional graphene datasets were analyzed to create orientation maps and generate images that isolate graphene thickness contrast. Graphene was used as the test sample due to its low scattering cross section, but the methods developed here should be generally applicable to any electron transparent sample, including 2D materials. Our belief is that the results published here will demonstrate diffraction-based characterization such as 4D STEM can be effectively employed in an SEM and that it will lead to wider adaptation by the SEM community.

Acknowledgments

We thank Ann Chiaramonti Debay for helpful microscopy related discussions and Mark Keller for providing some graphene samples and discussion that helped spur the development of this work. This work was performed while B.W.C. held a National Research Council Postdoctoral Associateship.

References

- [1] S. Z. Butler, S. M. Hollen, L. Cao, Y. Cui, J. A. Gupta, H. R. Gutiérrez, T. F. Heinz, S. S. Hong, J. Huang, A. F. Ismach, E. Johnston-Halperin, M. Kuno, V. V. Plashnitsa, R. D. Robinson, R. S. Ruoff, S. Salahuddin, J. Shan, L. Shi, M. G. Spencer, M. Terrones, W. Windl, J. E. Goldberger, *Progress, Challenges, and Opportunities in Two-Dimensional Materials Beyond Graphene*, ACS Nano 7 (4) (2013) 2898–2926. doi:10.1021/nn400280c. URL <http://pubs.acs.org/doi/10.1021/nn400280c>
- [2] P. Yasaei, A. Fathizadeh, R. Hantehzadeh, A. K. Majee, A. El-Ghandour, D. Estrada, C. Foster, Z. Aksamija, F. Khalili-Araghi, A. Salehi-Khojin, *Bimodal Phonon Scattering in Graphene Grain Boundaries*, Nano Letters 15 (7) (2015) 4532–4540. doi:10.1021/acs.nanolett.5b01100. URL <http://pubs.acs.org/doi/10.1021/acs.nanolett.5b01100>
- [3] A. W. Tsen, L. Brown, M. P. Levendorf, F. Ghahari, P. Y. Huang, R. W. Havener, C. S. Ruiz-Vargas, D. A. Muller, P. Kim, J. Park, *Tailoring Electrical Transport Across Grain Boundaries in Polycrystalline Graphene*, Science 336 (6085) (2012) 1143–1146. doi:10.1126/science.1218948. URL <http://www.sciencemag.org/cgi/doi/10.1126/science.1218948>
- [4] G.-H. Lee, R. C. Cooper, S. J. An, S. Lee, A. van der Zande, N. Petrone, A. G. Hammerberg, C. Lee, B. Crawford, W. Oliver, J. W. Kysar, J. Hone, *High-Strength Chemical-Vapor-Deposited Graphene and Grain Boundaries*, Science 340 (6136) (2013) 1073–1076. doi:10.1126/science.1235126. URL <http://www.sciencemag.org/cgi/doi/10.1126/science.1235126>
- [5] Z. Zhang, X. Zou, V. H. Crespi, B. I. Yakobson, *Intrinsic Magnetism of Grain Boundaries in Two-Dimensional Metal Dichalcogenides*, ACS Nano 7 (12) (2013) 10475–10481. doi:10.1021/nn4052887. URL <https://pubs.acs.org/doi/10.1021/nn4052887>
- [6] P. E. Batson, N. Dellby, O. L. Krivanek, *Sub-ångstrom resolution using aberration corrected electron optics*, Nature 418 (6898) (2002) 617–620. doi:10.1038/nature00972. URL <http://www.nature.com/articles/nature00972>
- [7] M. H. Gass, U. Bangert, A. L. Bleloch, P. Wang, R. R. Nair, A. K. Geim, *Free-standing graphene at atomic resolution*, Nature Nanotechnology 3 (11) (2008) 676–681. doi:10.1038/nnano.2008.280. URL <http://www.nature.com/articles/nnano.2008.280>
- [8] P. Y. Huang, C. S. Ruiz-Vargas, A. M. van der Zande, W. S. Whitney, M. P. Levendorf, J. W. Kevek, S. Garg, J. S. Alden, C. J. Hustedt, Y. Zhu, J. Park, P. L. McEuen, D. A. Muller, *Grains and grain boundaries in single-layer graphene atomic patchwork quilts*, Nature 469 (7330) (2011) 389–392. arXiv:1009.4714, doi:10.1038/nature09718. URL <http://www.nature.com/doi/10.1038/nature09718>
<http://www.nature.com/articles/nature09718>
- [9] K. Kim, Z. Lee, W. Regan, C. Kisielowski, M. F. Crommie, A. Zettl, *Grain Boundary Mapping in Polycrystalline Graphene*, ACS Nano 5 (3) (2011) 2142–2146. doi:10.1021/nn1033423. URL <http://pubs.acs.org/doi/10.1021/nn1033423>
- [10] Y. Han, K. Nguyen, M. Cao, P. Cueva, S. Xie, M. W. Tate, P. Purohit, S. M. Gruner, J. Park, D. A. Muller, *Strain Mapping of Two-Dimensional Heterostructures with Subpicometer Precision*, Nano Letters 18 (6) (2018) 3746–3751. arXiv:1801.08053, doi:10.1021/acs.nanolett.8b00952. URL <http://pubs.acs.org/doi/10.1021/acs.nanolett.8b00952>
- [11] C. Gammer, V. Burak Ozdol, C. H. Liebscher, A. M. Minor, *Diffraction contrast imaging using virtual apertures*, Ultramicroscopy 155 (2015) 1–10. doi:10.1016/j.ultramic.2015.03.015. URL <http://linkinghub.elsevier.com/retrieve/pii/S0304399115000649>
- [12] M. Konno, T. Ogashiwa, T. Sunaoshi, Y. Orai, M. Sato, *Lattice imaging at an accelerating voltage of 30kV using an in-lens type cold field-emission scanning electron microscope*, Ultramicroscopy 145 (2014) 28–35. doi:10.1016/j.ultramic.2013.09.001. URL <https://linkinghub.elsevier.com/retrieve/pii/S030439911300257X>
- [13] C. Sun, E. Müller, M. Meffert, D. Gerthsen, *On the Progress of Scanning Transmission Electron Microscopy (STEM) Imaging in a Scanning Electron Microscope*, Microscopy and Microanalysis 24 (02) (2018) 99–106. doi:10.1017/S1431927618000181. URL https://www.cambridge.org/core/product/identifier/S1431927618000181/type/journal_article
- [14] N. Brodusch, H. Demers, A. Gellé, A. Moores, R. Gauvin, *Electron energy-loss spectroscopy (EELS) with a cold-field emission scanning electron microscope at low accelerating voltage in transmission mode*, Ultramicroscopy 203 (2019) 21–36. doi:10.1016/j.ultramic.2018.12.015. URL <https://linkinghub.elsevier.com/retrieve/pii/S0304399118303255>
- [15] G. Arrighi, *The Global Market*, Journal of World-Systems Research 5 (2) (1999) 216–251. doi:10.5195/jwsr.1999.129. URL <http://jwsr.pitt.edu/ojs/jwsr/article/view/129>
- [16] H.-P. Komsa, J. Kotakoski, S. Kurasch, O. Lehtinen, U. Kaiser, A. V. Krashenninnikov, *Two-Dimensional Transition Metal Dichalcogenides under Electron Irradiation: Defect Production and Doping*, Physical Review Letters 109 (3) (2012) 035503. arXiv:1206.4407, doi:10.1103/PhysRevLett.109.035503. URL <https://link.aps.org/doi/10.1103/PhysRevLett.109.035503>
- [17] J. H. Choi, J. Lee, S. M. Moon, Y.-T. Kim, H. Park, C. Y. Lee, *A Low-Energy Electron Beam Does Not Damage Single-Walled Carbon Nanotubes and Graphene*, The Journal of Physical Chemistry Letters 7 (22) (2016) 4739–4743. doi:10.1021/acs.jpclett.6b02185. URL <http://pubs.acs.org/doi/abs/10.1021/acs.jpclett.6b02185>
<http://pubs.acs.org/doi/10.1021/acs.jpclett.6b02185>
- [18] L. Reimer, *Transmission Electron Microscopy*, Vol. 36 of Springer Series in Optical Sciences, Springer New York, New York, NY, 2008. doi:10.1007/978-0-387-40093-8. URL <http://link.springer.com/10.1007/978-0-387-40093-8>
- [19] B. W. Caplins, J. D. Holm, R. R. Keller, *Orientation mapping of graphene in a scanning electron microscope*, Carbon 149 (2019) 400–406. doi:10.1016/j.carbon.2019.04.042. URL <https://linkinghub.elsevier.com/retrieve/pii/S0008622319303768>
- [20] P. Schweizer, C. Dolle, E. Spiecker, *In situ manipulation and switching of dislocations in bilayer graphene*, Science Advances 4 (8) (2018) 1–7. doi:10.1126/sciadv.aat4712.
- [21] B. W. Caplins, J. D. Holm, R. R. Keller, *Transmission imaging with a programmable detector in a scanning electron microscope*, Ultramicroscopy 196 (2019) 40–48. doi:10.1016/j.ultramic.2018.09.006. URL <https://linkinghub.elsevier.com/retrieve/pii/S0304399118301578>
- [22] B. Caplins, J. D. Holm, R. R. Keller, *A programmable dark-field detector for imaging two-dimensional materials in the scanning electron microscope*, in: M. R. Douglass, B. L. Lee,

- J. Ehmke (Eds.), *Emerging Digital Micromirror Device Based Systems and Applications XI*, no. March 2019, SPIE, 2019, p. 13. doi:10.1117/12.2508694.
URL <https://www.spiedigitallibrary.org/conference-proceedings-of-spie/10932/2508694/A-programmable-dark-field-detector-for-imaging-two-dimensional-materials/crosscopy-datasets> (mar 2020). arXiv:2003.09523.
URL <http://arxiv.org/abs/2003.09523>
- [23] T. Sunaoshi, K. Kaji, Y. Orai, C. Schamp, E. Voelkl, STEM/SEM, *Chemical Analysis, Atomic Resolution and Surface Imaging At <= 30 kV with No Aberration Correction for Nanomaterials on Graphene Support*, *Microscopy and Microanalysis* 22 (S3) (2016) 604–605. doi:10.1017/S1431927616003871.
URL http://www.journals.cambridge.org/abstract/_jS1431927616003871
- [24] J. J. Fundenberger, E. Bouzy, D. Goran, J. Guyon, H. Yuan, A. Morawiec, *Orientation mapping by transmission-SEM with an on-axis detector*, *Ultramicroscopy* 161 (2016) 17–22. doi:10.1016/j.ultramic.2015.11.002.
URL <http://dx.doi.org/10.1016/j.ultramic.2015.11.002>
- [25] S. Vespucci, A. Winkelmann, K. Mingard, D. Maneuski, V. O'Shea, C. Trager-Cowan, *Exploring transmission Kikuchi diffraction using a Timepix detector*, *Journal of Instrumentation* 12 (02) (2017) C02075–C02075. doi:10.1088/1748-0221/12/02/C02075.
URL <http://stacks.iop.org/1748-0221/12/i=02/a=C02075?key=crossref.98acbbb8f0498c695acd23d4bfb11701>
- [26] H. Demers, N. Brodusch, R. Gauvin, *Low Accelerating Voltage Scanning Transmitted Electron Microscope: Imaging, Diffraction, X-ray Microanalysis, and Electron Energy-Loss Spectroscopy at the Nanoscale*, *Microscopy and Microanalysis* 23 (S1) (2017) 528–529. doi:10.1017/s1431927617003324.
- [27] S. Rudinsky, A. S. Sanz, R. Gauvin, *Wave-packet numerical investigation of thermal diffuse scattering: A time-dependent quantum approach to electron diffraction simulations*, *Micron* 126 (2019) 102737. doi:10.1016/j.micron.2019.102737.
URL <https://linkinghub.elsevier.com/retrieve/pii/S0968432819301489>
- [28] P. Schweizer, P. Denninger, C. Dolle, E. Spiecker, *Low Energy Nano Diffraction (LEND) – A versatile diffraction technique in SEM*, *Ultramicroscopy* (2020) 112956. doi:10.1016/j.ultramic.2020.112956.
URL <https://linkinghub.elsevier.com/retrieve/pii/S0304399119303183>
- [29] S. I. Wright, M. M. Nowell, R. de Kloe, P. Camus, T. Rampton, *Electron imaging with an EBSD detector*, *Ultramicroscopy* 148 (2015) 132–145. doi:10.1016/j.ultramic.2014.10.002.
URL <http://linkinghub.elsevier.com/retrieve/pii/S0304399114001946>
- [30] G. C. Sneddon, P. W. Trimby, J. M. Cairney, *Transmission Kikuchi diffraction in a scanning electron microscope: A review*, *Materials Science and Engineering R: Reports* 110 (2016) 1–12. doi:10.1016/j.mser.2016.10.001.
URL <http://dx.doi.org/10.1016/j.mser.2016.10.001>
- [31] W. C. Lenthe, J. C. Stinville, M. P. Echlin, Z. Chen, S. Daly, T. M. Pollock, *Advanced detector signal acquisition and electron beam scanning for high resolution SEM imaging*, *Ultramicroscopy* 195 (February) (2018) 93–100. doi:10.1016/j.ultramic.2018.08.025.
URL <https://doi.org/10.1016/j.ultramic.2018.08.025>
- [32] P. Hoess, K. Fleder, *Time-integrated phosphor behavior in gated image intensifier tubes*, *Image Intensifiers and Applications II* 4128 (November 2000) (2000) 23. doi:10.1117/12.405878.
- [33] J. Holm, *Scattering intensity distribution dependence on collection angles in annular dark-field STEM-in-SEM images*, *Ultramicroscopy* 195 (2018) 12–20. doi:10.1016/j.ultramic.2018.06.007.
URL <https://linkinghub.elsevier.com/retrieve/pii/S0304399118300482>
- [34] B. H. Savitzky, L. A. Hughes, S. E. Zeltmann, H. G. Brown, S. Zhao, P. M. Pelz, E. S. Barnard, J. Donohue, L. R. DaCosta, T. C. Pekin, E. Kennedy, M. T. Janish, M. M. Schneider, P. Herring, C. Gopal, A. Anapolsky, P. Ercius, M. Scott, J. Ciston, A. M. Minor, C. Ophus, *py4DSTEM: a software package for multimodal analysis of four-dimensional scanning transmission electron microscopy datasets* (mar 2020). arXiv:2003.09523.
URL <http://arxiv.org/abs/2003.09523>
- [35] M. Guizar-Sicairos, S. T. Thurman, J. R. Fienup, *Efficient sub-pixel image registration algorithms*, *Optics letters* 33 (2) (2008) 156–8.
URL <http://www.ncbi.nlm.nih.gov/pubmed/18197224>
- [36] J. Meyer, A. Geim, M. Katsnelson, K. Novoselov, D. Obergfell, S. Roth, C. Girit, A. Zettl, *On the roughness of single- and bi-layer graphene membranes*, *Solid State Communications* 143 (1-2) (2007) 101–109. doi:10.1016/j.ssc.2007.02.047.
URL <http://linkinghub.elsevier.com/retrieve/pii/S003810980700316X>
- [37] J. Liu, J. Lhermitte, Y. Tian, Z. Zhang, D. Yu, K. G. Yager, *Healing X-ray scattering images*, *IUCrJ* 4 (4) (2017) 455–465. doi:10.1107/s2052252517006212.
- [38] P. Kovesi, *Good Colour Maps: How to Design Them*, arxiv (2015) 1–42. arXiv:1509.03700.
URL <http://arxiv.org/abs/1509.03700>
- [39] Y.-C. Lin, C.-C. Lu, C.-H. Yeh, C. Jin, K. Suenaga, P.-W. Chiu, *Graphene Annealing: How Clean Can It Be?*, *Nano Letters* 12 (1) (2012) 414–419. doi:10.1021/nl203733r.
URL <http://pubs.acs.org/doi/10.1021/nl203733r>
- [40] X. Li, W. Cai, J. An, S. Kim, J. Nah, D. Yang, R. Piner, A. Velamakanni, I. Jung, E. Tutuc, S. K. Banerjee, L. Colombo, R. S. Ruoff, *Large-area synthesis of high-quality and uniform graphene films on copper foils*, *Science* 324 (5932) (2009) 1312–1314. arXiv:0905.1712, doi:10.1126/science.1171245.
- [41] L. Reimer, *Scanning Electron Microscopy*, Vol. 45 of Springer Series in Optical Sciences, Springer Berlin Heidelberg, Berlin, Heidelberg, 1998. doi:10.1007/978-3-540-38967-5.
URL <http://link.springer.com/10.1007/978-3-540-38967-5>
- [42] B. Zhang, J. Zerubia, *Point-Spread Function Models* 46 (10) (2007) 1819–1829.
- [43] L. Brown, R. Hovden, P. Huang, M. Wojcik, D. A. Muller, J. Park, *Twining and Twisting of Tri- and Bilayer Graphene*, *Nano Letters* 12 (3) (2012) 1609–1615. doi:10.1021/nl204547v.
URL <http://pubs.acs.org/doi/10.1021/nl204547v>
- [44] J. Ping, M. S. Fuhrer, *Layer Number and Stacking Sequence Imaging of Few-Layer Graphene by Transmission Electron Microscopy*, *Nano Letters* 12 (9) (2012) 4635–4641. doi:10.1021/nl301932v.
URL <http://pubs.acs.org/doi/10.1021/nl301932v>
- [45] H. M. Merklinger, *FOCUSING the VIEW CAMERA*, internet Edition, Dartmouth, Nova Scotia, 2007.
- [46] J. Goulden, P. Trimby, A. Bewick, *The Benefits and Applications of a CMOS-based EBSD Detector*, *Microscopy and Microanalysis* 24 (S1) (2018) 1128–1129. doi:10.1017/S1431927618006128.
URL https://www.cambridge.org/core/product/identifier/S1431927618006128/type/journal_article
- [47] T. Hase, T. Kano, E. Nakazawa, H. Yamamoto, *Phosphor Materials for Cathode-Ray Tubes*, *Advances in Electronics and Electron Physics* 79 (C) (1990) 271–373. doi:10.1016/S0065-2539(08)60600-9.
- [48] C. Ophus, *Four-Dimensional Scanning Transmission Electron Microscopy (4D-STEM): From Scanning Nanodiffraction to Ptychography and Beyond*, *Microscopy and Microanalysis* 25 (3) (2019) 563–582. doi:10.1017/S1431927619000497.
URL https://www.cambridge.org/core/product/identifier/S1431927619000497/type/journal_article
- [49] M. W. Tate, P. Purohit, D. Chamberlain, K. X. Nguyen, R. Hovden, C. S. Chang, P. Deb, E. Turgut, J. T. Heron, D. G. Schlom, D. C. Ralph, G. D. Fuchs, K. S. Shanks, H. T. Philipp, D. A. Muller, S. M. Gruner, *High Dynamic Range Pixel Array Detector for Scanning Transmission Electron*

- Microscopy, Microscopy and Microanalysis 22 (01) (2016) 237–249. doi:10.1017/S1431927615015664.
URL http://www.journals.cambridge.org/abstract/_jS1431927615015664
- [50] A. J. Wilkinson, G. Moldovan, T. B. Britton, A. Bewick, R. Clough, A. I. Kirkland, Direct detection of electron backscatter diffraction patterns, Physical Review Letters 111 (6) (2013) 1–5. doi:10.1103/PhysRevLett.111.065506.
 - [51] S. Vespucci, A. Winkelmann, G. Naresh-Kumar, K. P. Mingard, D. Maneuski, P. R. Edwards, A. P. Day, V. O’Shea, C. Trager-Cowan, Digital direct electron imaging of energy-filtered electron backscatter diffraction patterns, Physical Review B 92 (20) (2015) 205301. doi:10.1103/PhysRevB.92.205301.
URL <https://link.aps.org/doi/10.1103/PhysRevB.92.205301>
 - [52] T. Vystavěl, P. Stejskal, M. Unčovský, C. Stephens, Tilt-free EBSD, Microscopy and Microanalysis 24 (S1) (2018) 1126–1127. doi:10.1017/s1431927618006116.
 - [53] G. W. Adhyaksa, S. Brittman, H. Āboliņš, A. Lof, X. Li, J. D. Keelor, Y. Luo, T. Duevski, R. M. Heeren, S. R. Ellis, D. P. Fenning, E. C. Garnett, Understanding Detrimental and Beneficial Grain Boundary Effects in Halide Perovskites, Advanced Materials 30 (52) (2018) 1–9. doi:10.1002/adma.201804792.
 - [54] K. P. Mingard, M. Stewart, M. G. Gee, S. Vespucci, C. Trager-Cowan, Practical application of direct electron detectors to EBSD mapping in 2D and 3D, Ultramicroscopy 184 (2018) 242–251. doi:10.1016/j.ultramic.2017.09.008.